



We are Nitinol.™

## Crystalline-to-Amorphous Transitions in Ti-Ni Alloys

Pelton, Moine, Noack, Sinclair

Mat. Res. Soc. Symp. Proc.

Vol. 62

pp. 291-302

1986

## CRYSTALLINE-TO-AMORPHOUS TRANSITIONS IN Ti-Ni ALLOYS

A. R. PELTON\*, P. MOINE\*\* M. A. NOACK\*, and R. SINCLAIR\*\*\*  
\* Metallurgy and Ceramics Division, Ames Laboratory, Iowa State University,  
Ames, IA 50011  
\*\* Universite de Poitiers, Poitiers, France  
\*\*\* Dept. of Mat. Sci. and Engr., Stanford Univ., Stanford, CA 94305

## ABSTRACT

Ti-Ni alloys have been made amorphous over a broad composition range by sputter deposition, ion implantation and electron irradiation. Structural analysis of these alloys was made by electron diffraction techniques. Microdensitometer traces of diffraction patterns produced scattering profiles from which radial distribution functions (RDF's) were derived. The results from this analysis were comparable to those from x-ray diffraction studies on similar alloys. It was found that the positions of the intensity maxima vary systematically with alloy composition. However, values of coordination number were less precise due to experimental uncertainties. Furthermore, no dramatic differences were observed in the RDF's of the samples amorphized by the three techniques.

## INTRODUCTION

Currently, there is a wide interest in the structure and properties of metallic glasses. Novel techniques have been developed for both the synthesis and analysis of non-crystalline materials. For example, amorphous Ti-Ni has been synthesized by melt spinning [1,2], sputter deposition [3], ion implantation [4,5], and electron irradiation [6,7]. Among these techniques, the "effective" quench rate varies approximately six orders of magnitude [8]. It is therefore conceivable that different amorphous structures may attain from these methods. Structural information from metallic glasses is usually obtained by conventional x-ray or neutron diffraction techniques when sufficient quantities of material are available. However, ion implantation and electron irradiation are only capable of amorphizing thin surface layers. For these cases, selected-area electron diffraction patterns can provide high quality structural data. The purpose of this paper is twofold: (1) to review our recent results on the synthesis of amorphous Ti-Ni, and (2) to outline the procedure used to characterize amorphous structures by the analysis of electron diffraction patterns.

## EXPERIMENTAL PROCEDURE

We have used sputter deposition, ion implantation, and electron irradiation techniques to amorphize Ti-Ni alloys. The experimental details of these investigations have been published elsewhere [3-7]; therefore, only the salient details will be outlined here.

### Sputter Deposition

Samples were prepared by sputter deposition using two magnetron sources of elemental Ti and Ni targets. The deposition profiles of the two sources overlapped which produced a deposit with the composition varying monotonically from Ti-rich to Ni-rich. Deposition rates were in the range of 1.0-1.5 nm·sec<sup>-1</sup> with an argon gas sputtering atmosphere of 3 x 10<sup>-3</sup> T.

### Ion Implantation

Ti<sub>50</sub>Ni<sub>50</sub> TEM samples were Ni<sup>+</sup> implanted at room temperature with successive bombardment at decreasing energies of 250, 200, 100, and 50 keV. The corresponding doses were 2.79 x 10<sup>15</sup>, 2.16 x 10<sup>15</sup>, 1.23 x 10<sup>15</sup>, and 6.6 x 10<sup>14</sup> ions·cm<sup>-2</sup>. This implantation scheme produced a nearly flat ion concentration profile from 5.0 to 80 nm.

### Electron Irradiation

TEM samples were irradiated in the 1.5 MeV high voltage electron microscope (HVEM) at the National Center for Electron Microscopy in Berkeley. Several combinations of accelerating potential (0.5 to 1.5 MeV), beam currents (0.5 to 20 A cm<sup>-2</sup>), temperatures (90 to 300 K), alloy composition, and specimen orientations were used. Damage rates were calculated using damage cross sections ( $\sigma d$ ) from weighted mean values based on effective displacement threshold energy values of 30 eV for Ti and 40 eV for Ni [9]. At 1.5 MeV,  $\sigma d$  is approximately 27 barns; therefore, with a typical electron density of 3 x 10<sup>19</sup> e·cm<sup>-2</sup>·sec<sup>-1</sup>, the damage rate is 2.0 x 10<sup>-3</sup> dpa·sec<sup>-1</sup>.

### Transmission Electron Microscopy

Images and selected area diffraction patterns of the sputtered and ion-implanted amorphous samples were recorded on photographic film with 120 or 200 kV TEM's. These samples were then crystallized in situ with a heating stage, and the same regions were again recorded. The electron-irradiated samples were imaged at selected time intervals during the irradiation experiments. Several exposures were taken of each SADP to optimize the contrast levels for subsequent analysis. Microdensitometer traces of these diffraction negatives provided curves of raw intensity as a function of scattering angle,  $s (= 4 \sin \theta / \lambda)$ . Scattering data were collected up to  $s = 14 \text{ \AA}^{-1}$ .

## AMORPHOUS STRUCTURE ANALYSIS

### Background

Amorphous structures may be defined as atomic arrangements which do not possess any long-range periodicities but rather only short-range atomic order. Hence, diffraction patterns from amorphous alloys contain a series of broad maxima in contrast to the sharp lines observed for crystalline materials. This

broadening is due to both the variation of the first neighbor distance inherent in the amorphous structure and to the difference in atomic sizes. As such, diffraction data from amorphous structures provide only statistical information on the atomic structure. The usual method for representing amorphous structural data is with a radial distribution function (RDF). This function is a radial density of atoms averaged over all atoms taken at the origin. If  $\rho(r)$  is the local atomic density, then RDF( $r$ ) is  $4\pi r^2 \rho(r)$ . Integration of RDF( $r$ ) gives the average number of atoms at distances between  $r$  and  $r + \Delta r$  from the chosen origin. Additionally, positions of maxima in RDF( $r$ ) curves indicate frequently occurring atom-atom separations. It is these two parameters, i.e., coordination number and peak positions, which are used to characterize the amorphous structures.

The RDF( $r$ ) curves are derived from the scattering data; the analytical methods for these calculations are presented in the following section. In this report, we follow the formalism of Cargill [10] and Nandra and Grundy [11].

#### Analytical Method

The interference function is defined as:

$$I_m(s) = \frac{I_{N,obs}(s) - N\langle f^2 \rangle}{N\langle f \rangle^2}, \quad (1)$$

where  $N$  is the number of atoms, and for the Ti-Ni system,  $\langle f^2 \rangle = (x_{Ti} f_{Ti}^2 + x_{Ni} f_{Ni}^2)$  is the mean square scattering factor, and  $\langle f \rangle^2 = [(x_{Ti} f_{Ti} + x_{Ni} f_{Ni})^2]$  is the square of the mean scattering factor. The observed coherent scattering intensity,  $I_{N,obs}(s)$  is comprised of two contributions:

$$I_{N,obs}(s) = I_{obs}(s) - I_{incoh}(s). \quad (2)$$

$I_{obs}(s)$  is the raw scattering intensity from the microdensitometer traces, and  $I_{incoh}(s)$  includes corrections for absorption, polarization, multiple scattering, and incoherent scattering. It is therefore necessary to isolate the coherent scattering which will be used in the RDF calculations. In the absence of energy filtering [12], the term  $I_{incoh}(s)$  from equation 2 is assumed to be equivalent to the background intensity,  $I_{CB}(s)$ , of the crystalline SADP. As such, the interference function is

$$I_m(s) = \frac{I_{obs} - \alpha I_{CB} - \beta \langle f^2 \rangle}{\beta \langle f \rangle^2}. \quad (3)$$

The normalization constant  $\alpha$  takes into account an eventual difference in the overall density of the photographic negatives from the amorphous and crystalline films. The values of  $\alpha$  and  $\beta$  are adjusted such that the curve

$$I_m(s) = \alpha I_{CB}(s) + \beta \langle f^2 \rangle \quad (4)$$

passes midway through the maxima and minima of  $I_{obs}(s)$ , and coincides with  $I_{obs}(s)$  at large values of  $s$ . The zero-intensity level of the photographic negatives cannot be accurately determined. Therefore, a constant  $C$  is added to equation 4 such that

$$I_m(s) - \alpha I_{CB}(s) = \beta \langle f^2 \rangle + C. \quad (5)$$

For each value of  $\alpha$  ( $0.5 < \alpha < 1.2$ ),  $\beta$  and  $C$  are calculated by a least square method. The retained value of  $\alpha$  (and the corresponding  $\beta$  and  $C$ ) is that which minimizes the chi-square test. Corrections for multiple scattering were not attempted.

The radial distribution function is related to the interference function through the reduced radial distribution function,  $G(r)$ . This latter function is simply:

$$G(r) = 4\pi r [\rho(r) - \rho_0] = [RDF(r) - 4\pi r^2 \rho_0]/r \quad (6)$$

where  $\rho_0$  is the average atomic density.  $G(r)$  is calculated from the Fourier transform of  $I_m(s)$  as

$$G(r) = \frac{2}{\pi} \int_0^{s_{max}} s I_m(s) \exp(-Bs^2) \sin(sr) ds. \quad (7)$$

The term  $\exp(-Bs)$ , where  $B = 0.015$ , is a damping factor. The coordination number is calculated from the integral

$$N = \int_{r_0}^{r^1} RDF(r) dr \quad (8)$$

where  $r^1$  is the first minimum after the first maximum in the function  $RDF(r) - 4\pi r^2 \rho_0$ . Furthermore, non-linearity effects in the photographic negatives at large values of  $s$  produce inaccuracies in  $I_m(s)$ . Due to these experimental uncertainties, the integral was terminated at  $s \sim 10 \text{ \AA}^{-1}$ . According to Waseda [13] the positions of the resultant ghost peaks are functions of the upper limit of integration, i.e.,  $s_{max}$ . These ghost maxima should appear at distances  $\Delta r = \pm 5\pi/2s_{max} = \pm 9\pi/2s_{max}$  from the main peak.

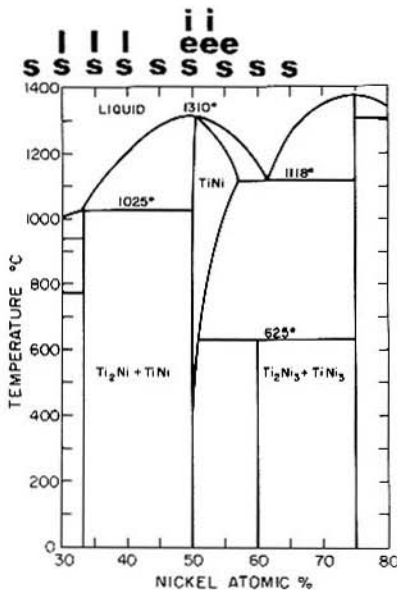


Figure 1: Partial Ti-Ni phase diagram which shows the composition ranges of amorphous alloys produced by sputtering (s), electron irradiation (e), and ion implantation (i) from this study, and by liquid quenching (l) from references 1 and 2.

## RESULTS AND DISCUSSION

### Compositions of Amorphous Ti-Ni Alloys

The partial Ti-Ni phase diagram in Figure 1 illustrates the composition ranges which have been made amorphous by sputter deposition (s), ion-implantation (i), and electron irradiation (e). The amorphous Ti-Ni alloy range for liquid quenching (l) [1,2] is also shown. Specifically, amorphous alloys from sputter deposition were observed in the broad composition range of 25-65 at.% Ni. This may be compared to the rather limited composition range of 30-40 at.% Ni by liquid quenching. Other alloy systems show this same trend, which can be attributed to the faster "effective" quench rate of sputter deposition. This also holds for the ion- and electron-irradiated specimens. Turnbull [8] estimated rapid liquid quench rates to be on the order of  $10^5$  to  $10^8$  K·sec<sup>-1</sup>, whereas, the "quench" rates for sputtering and irradiation are approximately  $10^{12}$  K·sec<sup>-1</sup>. For sputtered materials, this rate is based on the arrival time of the atoms, whereas, for irradiated samples, it is proportional to the time required for restoration of local thermal equilibrium following the implantation.

As is seen in Figure 1 the compositions of the irradiated samples are near Ti<sub>50</sub>Ni<sub>50</sub> which correspond to the composition range of the crystalline alloys which exhibit the shape-memory effects. Some applications of these shape-memory alloys require exposure to hostile environments such as for bio-medical

applications and in nuclear reactors. Recent results indicate that corrosion [14] and wear [15] resistance of ion-implanted  $Ti_{50}Ni_{50}$  with an amorphous surface layer is improved over those properties of fully crystalline materials.

### Microstructures

A bright-field image and selected-area diffraction pattern of an amorphous sputtered  $Ti_{44}Ni_{56}$  specimen is shown in Figure 2a. The microstructure is characterized by a typical mottled appearance of amorphous materials. Structural inhomogeneities (e.g. small crystallites) were not observed in these films by either amplitude- or phase-contrast imaging techniques. The SADP is also typical of amorphous structures, and reveals three diffuse rings. In situ crystallization of this sample at 550°C produced the microstructure seen in Figure 2b. This is a mixture of the B2 phase, (ordered bcc)  $Ni_3Ti$  ( $DO_{24}$  structure) and Phase X [3]. The crystal structure of this latter phase has not been fully determined; however, it appears to be a metastable Ni-rich phase with a distorted fcc structure and a lattice parameter of 15.93 Å [16]. Additional details of the crystallization behavior of these sputtered films is presented by Kim, et al. [17].

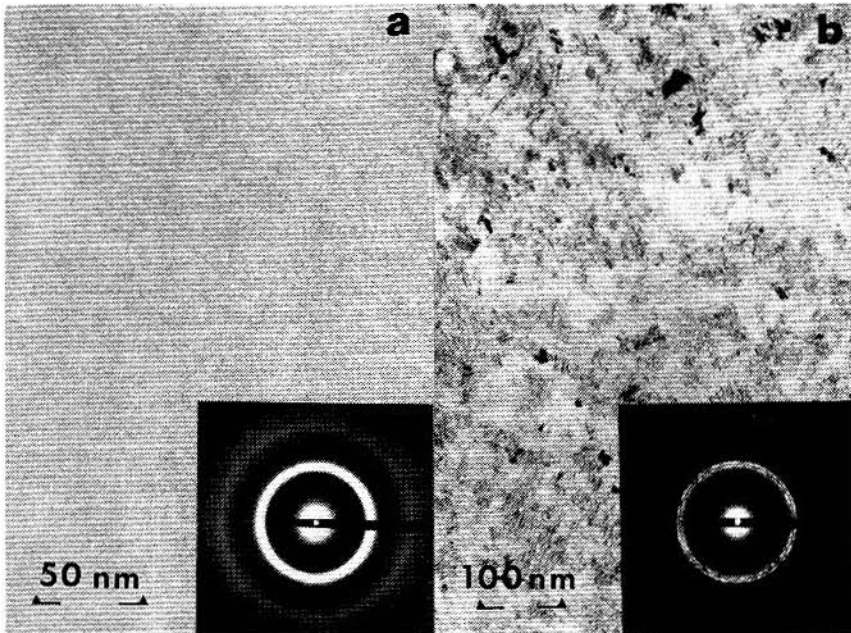


Figure 2: Microstructures and diffraction patterns of sputter-deposited  $Ti_{44}Ni_{56}$  before (a) and after (b) in situ crystallization.

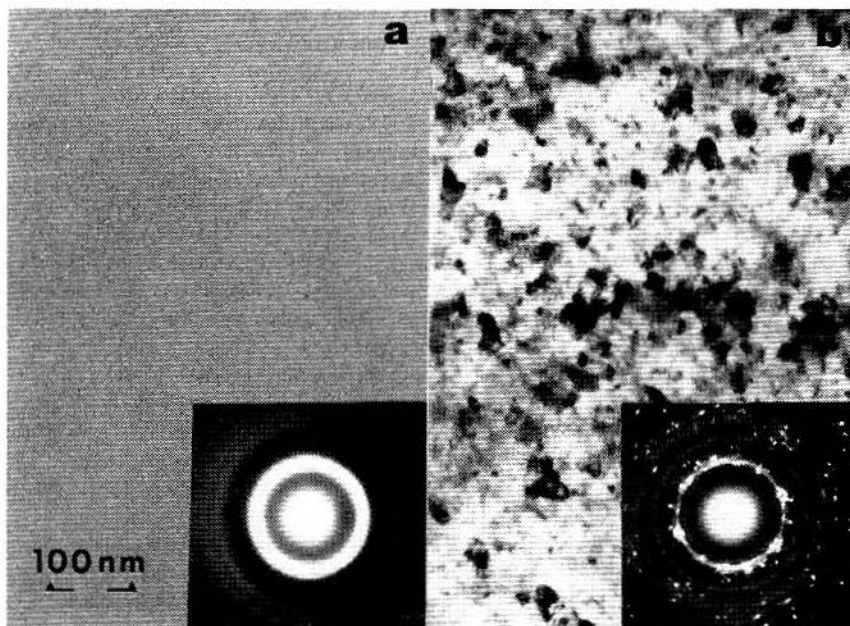


Figure 3; Microstructures and diffraction patterns of ion-implanted  $\text{Ti}_{50}\text{Ni}_{50}$  before (a) and after (b) in situ crystallization.

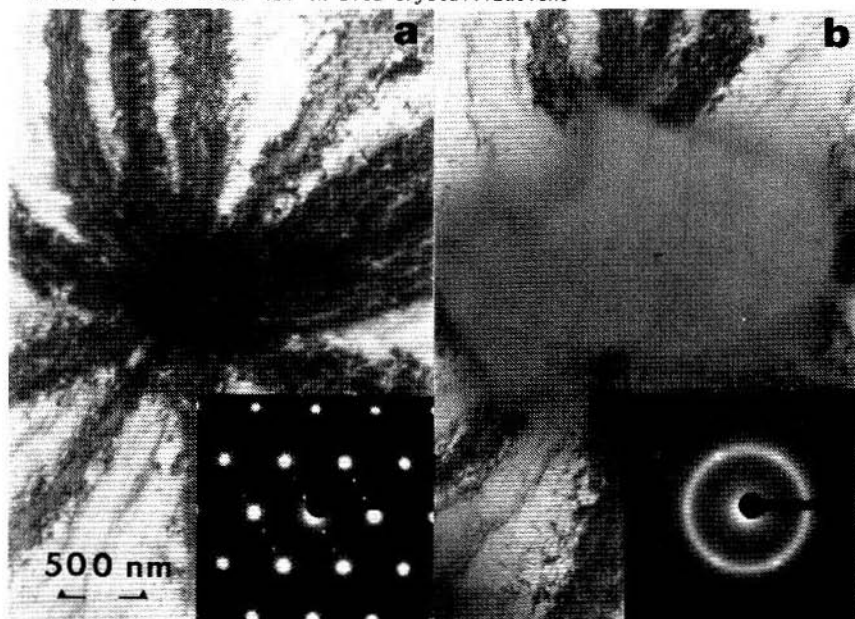


Figure 4: Microstructures and diffraction patterns of  $\text{Ti}_{50}\text{Ni}_{47}\text{Fe}_3$  before (a) and after (b) electron irradiation at 500 kV.

The as-implanted and re-crystallized microstructures of  $Ti_{50}Ni_{50}$  are shown in Figures 3a and 3b, respectively. This sample was implanted with  $Ni^+$  ions to a dose of  $7 \times 10^{15}$  ions $\cdot$ cm $^2$ , and was subsequently crystallized in situ at 550°C to form the R-phase, which is a rhombohedral distortion of B2 [18]. The nature of the ion ( $Ni^+$ ,  $Si^+$ ,  $Fe^+$ ,  $N^+$ ) does not appear to influence the crystalline to amorphous transformation in these alloys. The minimum dose for amorphization with  $Ni^+$  is  $5 \times 10^{12}$  ion $\cdot$ cm $^{-2}$  which corresponds to  $3 \times 10^{-2}$  dpa.

Figure 4 shows the images and diffraction patterns from a  $Ti_{50}Ni_{47}Fe_3$  sample before and after electron irradiation at 500 kV and 90 K. The initial structure is R-phase, which became amorphous after approximately ten minutes. Under these conditions, the total dose was  $\sim 10^{20}$  e $\cdot$ cm $^{-2}$  which corresponds to approximately  $10^{-2}$  dpa. The degree of amorphicity was monitored by the degradation of the extinction contours and the simultaneous appearance of diffuse rings in the SADP.

Previous investigations have shown that near equi-atomic Ti-Ni alloys readily become amorphous upon electron irradiation with a HVEM [6,7]. Two factors which greatly influence this crystalline-to-amorphous transformation are accelerating potential of the HVEM and sample temperature [7]. The kinetics of the transformation are increased with higher voltage ( $> 1.0$  MeV) and lower temperatures ( $< 150$  K).

The amorphous structures of the three samples qualitatively appear to be similar. In the next section we will present the results of the analysis of these diffraction patterns to allow quantitative comparisons to be made.

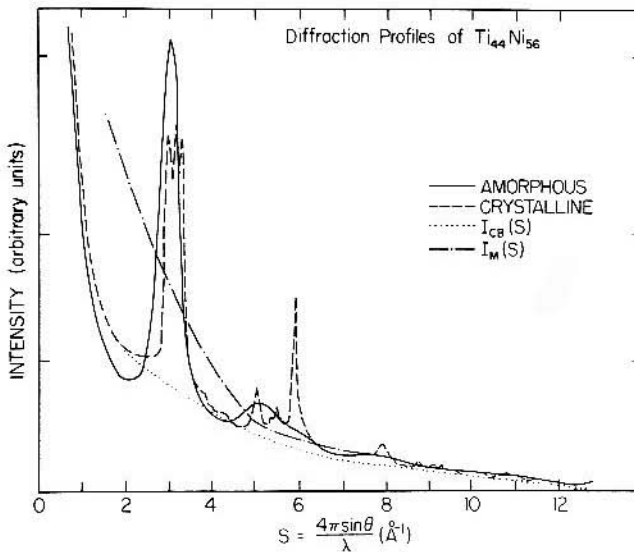


Figure 5: Intensity profiles of amorphous and crystallized diffraction patterns of sputtered  $Ti_{44}Ni_{56}$ .

### Electron Diffraction Pattern Analysis

The starting point in this analysis is to convert the diffraction intensities on the negatives to intensity versus scattering-angle curves. A typical analogue output from the microdensitometer trace is shown in Figure 5 for the amorphous and crystallized states of sputtered  $Ti_{44}Ni_{56}$ . These traces correspond to the conditions of Figure 2. Also shown are the crystalline background curve  $I_{CB}(s)$  and the fitted scattered intensity curve  $I_m(s)$ . Accurate calibration of the abscissa was made by indexing the crystalline diffraction pattern.

The interference functions for the three samples were calculated from equations 3-5, and the resultant curves are shown in Figure 6. These curves are quite similar in terms of overall shape, peak positions, and intensities. The shape is typical of many metallic glasses; in particular, the shoulder on the second peak is a fundamental characteristic. These results indicate that the amorphous structure may be modeled as dense random packing of hard spheres [10]. The peak position values from the interference functions are presented in Table I. Also included in this table are the results from x-ray diffraction experiments with  $MoK\alpha$  radiation. The first maximum of the sputtered  $Ti_{44}Ni_{56}$  sample has a peak position at  $3.0\text{\AA}^{-1}$  with both x-ray and electron diffraction. The other peak positions in this specimen are also nearly identical. However, the peak positions in the ion-implanted and electron-irradiated samples are slightly less than those of the sputtered film. Specifically, the first peak appears at 2.95 and  $2.92\text{\AA}^{-1}$ , respectively. These results also compare favorably with those reported by Wagner, et al. [20] on x-ray diffraction studies of melt-spun  $Ti_{65}Ni_{35}$  metallic glasses. For example, the shape of the interference function curves from the two studies is similar in the range  $2-6\text{\AA}^{-1}$ . Furthermore, they observed the first two maxima in the interference function at 2.85 and  $4.85\text{\AA}^{-1}$ . These small shifts in peak position may reflect the difference in compositions used in the two studies. The effect of composition on diffraction maxima position is a function of atomic sizes of the alloy constituents. The Goldschmidt diameter of Ti atoms is  $2.95\text{\AA}$  compared with  $2.5\text{\AA}$  for Ni. Thus, the Ti-rich glasses should have lower peak position values in the interference functions and correspondingly higher values in the distribution functions than Ni-rich metallic glasses. Our preliminary results on

TABLE I: CALCULATED STRUCTURE DATA

SPECIMEN	DIFFRACTION TECHNIQUE	$I_m(s)$ PEAK POSITIONS ( $\text{\AA}^{-1}$ )		RDF( $r$ ) PEAK POSITIONS ( $\text{\AA}$ )		COORDINATION NUMBER
		$s_1$	$s_2$	$r_1$	$r_2$	
Sputtered $Ti_{44}Ni_{56}$	X-Ray	3.0	5.2	2.58	4.5	13.2
	Electron	3.0	5.2	2.57	4.5	13.0
Ni <sup>+</sup> Implanted $Ti_{50}Ni_{50}$	Electron	2.95	5.1	2.58	4.5	13.4
Electron Irradi- ated (500 kV) $Ti_{50}Ni_{47}Fe_3$	Electron	2.92	5.1	2.61	4.5	14.6

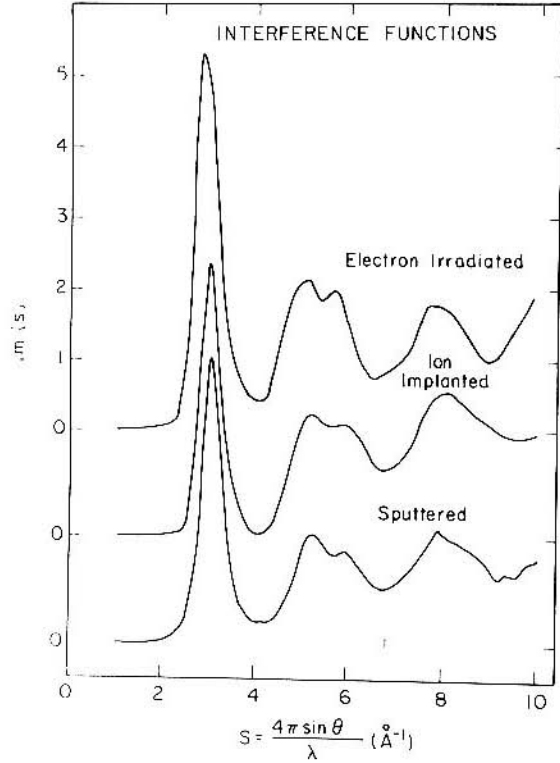


Figure 6: Interference functions of sputtered  $\text{Ti}_{44}\text{Ni}_{56}$ , ion-implanted  $\text{Ti}_{50}\text{Ni}_{50}$ , and electron-irradiated  $\text{Ti}_{50}\text{Ni}_{47}\text{Fe}_3$ .

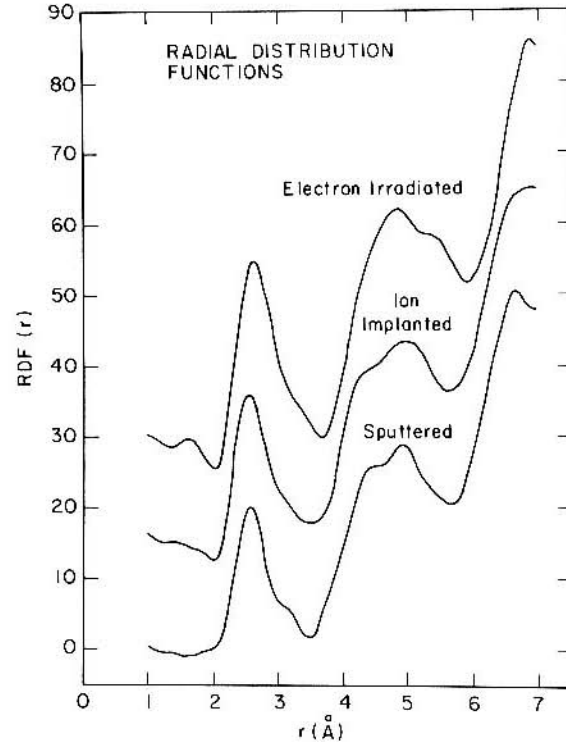


Figure 7: Radial distribution functions of sputtered  $\text{Ti}_{44}\text{Ni}_{56}$ , ion implantation  $\text{Ti}_{50}\text{Ni}_{50}$  and electron-irradiated  $\text{Ti}_{50}\text{Ni}_{47}\text{Fe}_3$ .

sputtered  $Ti_{30}Ni_{70}$  indicate a first maximum in the interference function at  $2.87\text{\AA}^{-1}$ . This is certainly consistent with the predicted trend.

Additional structural information is revealed from inspection of the RDF(r) curves in Figure 7 and the compilation of data in Table I. These curves are also characteristic of diffraction studies of metallic glasses. The positions of the first peak range from 2.58Å for  $Ti_{44}Ni_{56}$  (from both x-ray and electron diffraction) to 2.61Å for electron-irradiated  $Ti_{50}Ni_{47}Fe_3$ . The first peaks in these curves are rather broad and non-symmetric. This is likely to be an effect of the termination satellites as discussed earlier. These errors are reflected in the calculated coordination numbers, N, which are listed in Table I. N is approximately 13 for the sputtered and ion-implanted samples and greater than 14 for the electron-irradiated samples. These values may be compared to the global coordination number,  $N_{nn}$ , of  $Ti_{40}Ni_{60}$  which ranges from 12.1 to 12.8 [21].

Hence, there are no dramatic differences in the radial distribution functions of the samples discussed here which could be attributed to differences in the amorphization processes. This is a somewhat surprising result since the synthesis techniques are vastly different. Furthermore, the displacement mechanisms for ion and electron irradiation differ (e.g. there are no cascades with electrons). It was therefore thought that high voltage electrons would induce a more homogeneous damage state than would ion implantation [22]. If this were so, the electrons could destroy the long-range crystalline periodicities, but not necessarily the short-range order [19]. This could result in a change in the coordination number. Unfortunately, the data from the electron-irradiated sample was not deemed precise enough to provide a basis for comparison. However, these results indicate that the degree of amorphicity is not path dependent. Additional results from other compositions and treatments are forthcoming.

#### ACKNOWLEDGMENT

This work was initially supported by the NSF-MRL Program at Stanford University. Continued support for A. R. Pelton, M. A. Noack, and P. Moine (summer) is by the U.S.D.O.E. at Ames Laboratory, which is operated by Iowa State University under contract no. W-7405-Eng-82, supported by the Director of Energy Research, Office of Basic Energy Sciences. The authors thank D. Ackland and Dr. K. H. Westmacott for their help and advice with the HVEM. We also acknowledge collaborative work with Dr. J. L. Brimhall and assistance from F. C. Laabs.

#### REFERENCES

1. L.E. Tanner and R. Ray, U.S. Patent Nos. 4,126,449 and 4,148,669.
2. D.E. Polk, A. Calka and B.C. Giessen, *Acta Metall.* **26**, 1097 (1978).
3. A.R. Pelton, A.F. Marshall, and Y.S. Lee, *Proc. Ann. EMSA Meeting* **48**, 270 (1983).
4. P. Moine, J.P. Eymery, R.J. Gaboriaud and J. Delafond, *Nucl. Instr. and Methods* **209/210**, 267 (1983).

5. J.L. Brimhall, H.E. Kissinger, and L.A. Charlot, in Metastable Materials Formation by Ion Implantation, edited by S.T. Picraux and W.J. Choyke (North-Holland, New York, 1982), pp. 235-242; P. Moine, M.P. Riviere, N. Junqua, and J. Delafond, ibid., pp. 243-251.
6. G. Thomas, H. Mori, H. Fujita, and R. Sinclair, Scripta Met. 16, 589 (1982).
7. H. Fujita, H. Mori, and M. Fujita, Proc. of the 7th Int. Conf. on HVEM, edited by R.M. Fisher, R. Gronsky, and K.H. Westmacott (U.C. Berkeley Press, 1983), pp. 233-238; A.R. Pelton, ibid., pp. 245-250.
8. D. Turnbull, Met. Trans. 12A, 695 (1981).
9. T.A. Gabriel, B.C. Bishop, and F.W. Wiffen, ORNL Report ORNL/TM-6361.
10. G.S. Cargill, III, in Solid State Physics, edited by F. Seitz, D. Turnbull, and H. Ehrenreich (Academic Press, New York, 30 1975), pp. 227-320.
11. S.S. Nandra and P.J. Grundy, J. Phys: Metal Phys. 7, 207 (1977).
12. D.B. Dove, in Physics of Thin Films, edited by G. Hass, M.H. Francombe, R.W. Hoffman (Academic Press, New York, 1973), pp. 1-41.
13. Y. Waseda, The Structure of Non-crystalline Materials, (McGraw-Hill, New York, 1980), pp. 34-40.
14. R. Wang and J.L. Brimhall, MRS Symp. Proc. 27, 729 (1984).
15. P. Moine, U. Popoola, and J.P. Villain, submitted to Scripta Met.
16. J. Beyer, PhD Thesis, Technische Hogeschool Twente, The Netherlands, 1982.
17. J.J. Kim, D.L. Stevenson, and P. Moine, Scripta Met., accepted for publication (1985).
18. P. Moine, E. Goo, and R. Sinclair, Scripta Met. 18, 1143 (1984).
19. A.R. Pelton, P. Moine, and R. Sinclair, Proc. Ann. EMSA Meeting 42, 508 (1984).
20. C.N.J. Wagner, D. Lee, L. Keller, L.E. Tanner, and H. Ruppertsberg, Proc. Int. Conf. on Rapidly Quenched Metals 4, 331 (1981).
21. C.N.J. Wagner, Acta Met., accepted for publication (1985).
22. J.L. Brimhall, H.E. Kissinger, and A.R. Pelton, Proc. MRS 27, 163 (1983).